Thermal Design Methodology for High-Heat-Flux Single-Phase and Two-Phase Micro-Channel Heat Sinks

Weilin Qu and Issam Mudawar

Abstract—This paper explores several issues important to the thermal design of single-phase and two-phase micro-channel heat sinks. The first part of the paper concerns single-phase heat transfer in rectangular micro-channels. Experimental results are compared with predictions based on both numerical as well as fin analysis models. While the best agreement between predictions and experimental results was achieved with numerical simulation, a few of the fin models are found to provide fairly accurate predictions. The second part of the paper focuses on predicting the incipient boiling heat flux. A comprehensive model based on bubble departure and superheat criteria is developed and validated with experimental data. The incipience model is capable of predicting the location, shape and size of bubbles departing in rectangular micro-channels. In the third part of the study, an analytical model is developed to predict pressure drop across a two-phase micro-channel heat sink. This model provides a detailed assessment of pressure drop concerns with two-phase micro-channels, including compressibility, flashing and choking. Overall, the present study provides important guidelines concerning practical implementation of micro-channel heat sinks in high-heat-flux electronic cooling applications.

Index Terms—Boiling, boiling incipience, heat sink, high heat flux, micro-channel, phase change, pressure drop.

NOMENCLATURE

A_a	Area of micro-channel bottom wall, m^2.
A_b	Area of micro-channel sidewall, m^2.
A_c	Cross-sectional area of micro-channel, m^2.
A_{eff}	Effective area for heat transfer along micro-channel wall, m^2.
A_p	Projected area of bubble, m^2.
A_t	Planform area of heat sink top surface, m^2.
C_d	Drag coefficient in (14).
c_p	Specific heat at constant pressure, $kJ/kg \cdot^\circ C$.
C_s	Empirical coefficient in (19).
d_h	Hydraulic diameter of micro-channel, m.
e	Point half-way from nucleation site to bubble tip.
f	Friction factor.
F_d	Drag force, N.
F_s	Surface tension force, N.
G	Micro-channel mass velocity, $kg/m^2 \cdot s$.
h	Enthalpy, J/kg.
h_{ave}	Average convection heat transfer coefficient, $W/m^2 \cdot^\circ C$.
h_b	Height of bubble, m.
H_{cell}	Height of unit cell, m.
H_{ch}	Height of micro-channel, m.
h_e	Distance from point e to wall or corner, m.
h_{fg}	Latent heat of vaporization, J/kg.
H_{tc}	Distance from thermocouple to micro-channel bottom wall, m.
H_{w1}	Thickness of cover plate, m.
H_{w2}	Distance from unit cell bottom wall to micro-channel bottom wall, m.
k	Thermal conductivity, $W/m \cdot^\circ C$.
L	Length of micro-channel, m.
L_1, L_2, L_3, L_4	Distance between thermocouple holes, m.
M	Two-phase Mach number.
m	Fin parameter, 1/m.
N	Number of micro-channels in heat sink.
Nu	Micro-channel Nusselt number.
P	Pressure, *bar*.
P_c	Length of bubble contact line, m.
P_{in}	Micro-channel inlet pressure, *bar*.
P_{out}	Micro-channel outlet pressure, *bar*.
P_w	Total power input, W.
Pr	Prandtl number.
Q	Volume flow rate, m^3/s.
q''_{eff}	Heat flux based on heat sink top planform area, W/cm^2.
$q''_{eff,i}$	Incipient boiling heat flux based on heat sink top planform area, W/cm^2.
R	Thermal resistance, $^\circ C/W$.
r_b	Radius of departing bubble, m.
Re	Reynolds number of micro-channel.
Re_b	Bubble Reynolds number.
T	Temperature, $^\circ C$.
T_{in}	Micro-channel inlet temperature, $^\circ C$.
T_{out}	Micro-channel outlet temperature, $^\circ C$.
T_{sat}	Saturation temperature, $^\circ C$.
T_{tc1} to T_{tc4}	Thermocouple readings, $^\circ C$.
U	Dimensionless axial velocity.

u	Axial velocity, m/s.
u_e	Axial velocity at half-way point e, m/s.
u_{in}	Micro-channel inlet velocity, m/s.
u_{out}	Micro-channel outlet velocity, m/s.
v	Specific volume, m^3/kg.
V	Velocity vector, m/s.
v_{fg}	Specific volume difference between saturated vapor and saturated liquid, m^3/kg.
W	Width of heat sink top planform area, m.
W_{cell}	Width of unit cell, m.
W_{ch}	Width of micro-channel, m.
W_w	Half-width of wall separating micro-channels, m.
x	Cartesian coordinate.
x_e	Thermodynamic equilibrium quality.
x^*	Dimensionless thermal entry distance.
y	Cartesian coordinate.
Y	Dimensionless Cartesian coordinate.
z	Cartesian coordinate.
Z	Dimensionless Cartesian coordinate.

Greek Symbols:

α	Aspect ratio.
η	Fin efficiency.
θ	Dimensionless temperature.
θ_0	Equilibrium contact angle, *rad*.
θ_a	Advancing contact angle, *rad*.
θ_r	Receding contact angle, *rad*.
μ	Dynamic viscosity, N $\cdot$ s/m^2.
ρ	Density, kg/m^3.
σ	Surface tension, N/m.

Subscripts:

a	Micro-channel bottom wall.
air	Air.
ave	Average.
cap	Capacity.
$cond$	Conduction.
g	Vapor.
f	Liquid.
fin	Fin.
in	Micro-channel inlet.
l	Lexan cover.
out	Micro-channel exit.
s	Solid (oxygen-free copper).
sp	Single-phase.
tc	Thermocouple.
tp	Two-phase.

I. INTRODUCTION

MICRO-CHANNEL heat sinks constitute a powerful means for dissipating large amounts of heat from small surfaces. They possess several unique attributes that make them prime contenders for the next generation of coolers for high performance computer processors and laser diodes. A typical heat sink contains a large number of small diameter coolant channels. Liquids such as water and fluorochemicals are two types of coolant that are favored with micro-channel heat sinks. Heat sinks are classified into single-phase or two-phase according to whether boiling of liquid occurs inside the micro-channels.

Single-phase micro-channel heat sinks have been studied quite extensively during the last two decades [1]–[15]. Heat sinks with different substrate materials and dimensions have been fabricated and tested with various cooling liquids. Test results have demonstrated several technical merits of single-phase micro-channel heat sinks, namely, the ability to produce very large heat transfer coefficients, small size and volume per heat load, and small coolant inventory requirements [1]–[6]. In addition to experimental work, several theoretical studies can be found in the literature [7]–[15]. One of the primary objectives of these studies is to develop heat transfer modeling tools that are essential to the design and optimization of heat sink geometry. Two different approaches have been adopted: the fin analysis method and the numerical method. In the fin analysis method, the solid walls separating micro-channels are modeled as thin fins. Heat transfer analysis of the heat sink is greatly simplifies by introducing such approximations as one-dimensional heat transfer along the fins, constant convective heat transfer coefficient, and uniform fluid temperature [7]–[11]. The numerical method, on the other hand, involves detailed solution of the governing momentum and energy equations using numerical techniques [12]–[15].

Two-phase micro-channel heat sinks offer the same attributes as their single-phase counterparts while providing the following important added benefits: higher convective heat transfer coefficients, better temperature uniformity, and smaller coolant flow rates. Several aspects of fluid flow and boiling in two-phase micro-channel heat sinks have been investigated, namely, boiling incipience [16], pressure drop [17]–[20], bubble activity and flow patterns [20], [21], heat transfer characteristics [17]–[19], [22], [23], and critical heat flux (CHF) [17], [18]. Most two-phase studies are experimental and very few are dedicated to modeling.

The aforementioned studies provide valuable insight into the heat transfer characteristics in both single-phase and two-phase micro-channel heat sinks. However, our understanding remains quite limited, considering the lack of reliable predictive tools for practical heat sink design. In this study, several fundamental and practical issues important to the thermal design of micro-channel heat sink are discussed, and experiments were performed to assess the predictive capabilities of different models. These technical issues are linked together by a series of events associated with the transition from single-phase liquid cooling to flow boiling. In micro-channel heat sinks, the coolant remains in liquid state under conditions of high liquid flow rate or low heat flux. In the first part of this paper, single-phase experimental results are compared with predictions based on both the numerical method and several previous fin analysis methods. Decreasing liquid flow rate or increasing input heat flux will eventually lead to incipient boiling in micro-channels with the formation of a few vapor bubbles near the channel exit. Incipient boiling is an important parameter in heat sink design since it constitutes the upper design limit for heat sinks that are intended for single-phase liquid cooling only, and a lower limit for two-phase heat sinks indented for maximum heat dissipation. The second part of this study concerns both
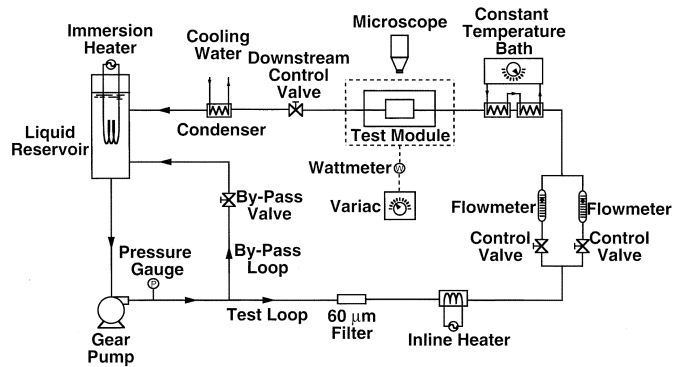
Fig. 1. Flow loop.

measurement and prediction of incipient boiling heat flux in a micro-channel heat sink. With a further decrease in liquid flow rate or increase in heat flux, flow boiling becomes more prevalent as a liquid-vapor mixture occupies a significant portion of the channel length. In the third part of this paper, an analytical model is presented to determine pressure drop for water flow boiling in a micro-channel heat sink, including compressibility, flashing, and choking effects.

II. MICRO-CHANNEL HEAT SINK FACILITY

A. Flow Loop

Fig. 1 shows the flow loop that was constructed to condition the working fluid, deionized water, to the desired micro-channel heat sink flow rate, inlet temperature, and outlet pressure. The water was pumped through the loop via a magnetically coupled gear pump. Only a portion of the pumped fluid entered the heat sink; the balance was bypassed. Upstream of the test module containing the heat sink were a filter, an inline heater, two parallel rotameters, and a constant temperature bath. The inline heater and constant temperature bath brought the water to the desired test module inlet temperature. Outlet pressure control was achieved by a throttling valve located downstream from the test module, which was followed by a heat exchanger to condense any vapor exiting the test module before the water returned to the reservoir.

B. Test Module

Fig. 2 illustrates the construction of the test module, which consisted of a micro-channel heat sink, housing, cover plate, and twelve cartridge heaters. The micro-channel heat sink was fabricated from a single block of oxygen-free copper. The planform (top) surface of the heat sink was 1.0 cm wide and 4.48 cm long. Twenty-one equidistantly spaced rectangular micro-slots, 231 μm in width and 712 μm in depth, were machined within the 1-cm width of the top surface. Four Type-K thermocouples were inserted below the heat sink top surface to measure the axial temperature distribution inside the heat sink. Twelve holes were drilled into the bottom of the heat sink to accommodate the cartridge heaters. These cartridge heaters were powered by a single 0–110 VAC variac, and their total power dissipation was measured by a precision wattmeter. Three thin slots were cut from the bottom surface up through most of the heat sink's height to reduce longitudinal heat spread within the heat sink.
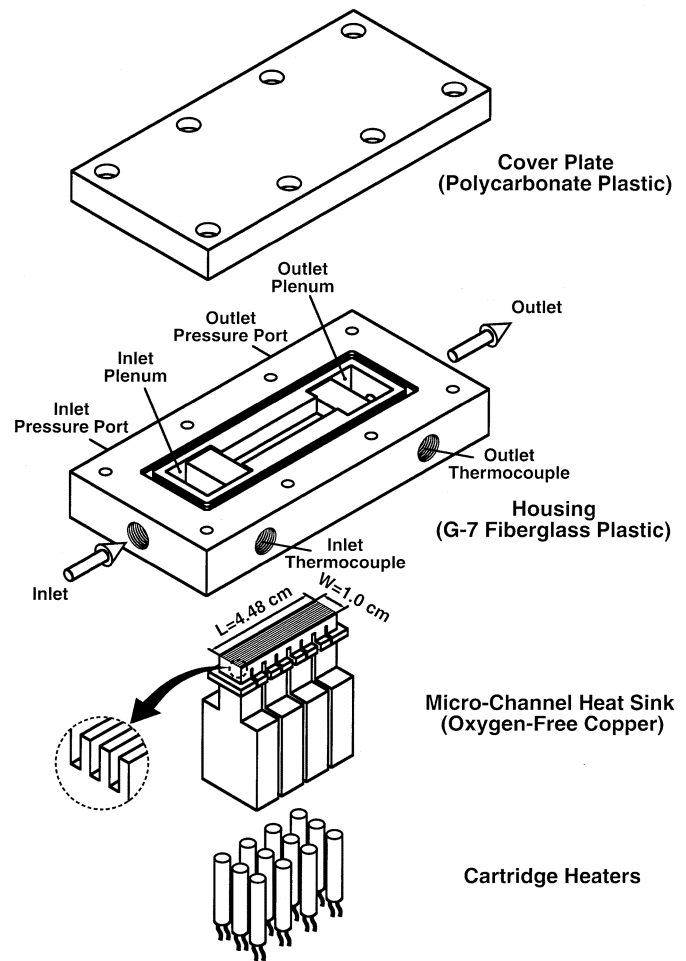
Fig. 2. Test module construction.

The heat sink housing was made from G-7 fiberglass plastic. The central part of the housing was removed where the heat sink was inserted. A small protruding platform machined around the periphery of the heat sink ensured the top surface of the heat sink was flush with the top surface of the housing. The housing contained plenums both upstream and downstream of the micro-channels as shown in Fig. 2. Two absolute pressure transducers were connected to the plenums to measure the inlet and exit pressures. Also located in the plenums were two Type-K thermocouples to measure the inlet and exit temperatures.

A cover plate made from transparent polycarbonate plastic (Lexan) was bolted atop the housing. The cover plate and micro-slots in the heat sink top surface formed closed micro-channels. A microscope was positioned above the cover plate to observe bubble activity inside the micro-channels as shown in Fig. 1.

C. Measurement Uncertainty

Measurement uncertainties associated with the wattmeter, rotameters, and pressure transducers were less than 0.5, 4, and 3.5%, respectively. The uncertainty associated with the thermocouple measurements was smaller than 0.3 °C. Heat loss to the ambient was estimated at less than 1% of the total power input; the cartridge heater power measured by the wattmeter was therefore used for all heat flux calculations.

TABLE I
OPERATING CONDITIONS FOR SINGLE-PHASE TESTS

Cooling liquid	Inlet temperature, T_{in} (°C)	Inlet velocity, u_{in} (m/s)	Effective heat flux, q''_{eff} (W/cm²)
Deionized water	15.0	0.45-5.48	100
	15.0	1.25-4.14	200

III. HEAT TRANSFER CHARACTERISTICS OF SINGLE-PHASE MICRO-CHANNEL HEAT SINK

A. Experimental Procedure

The operating conditions for the single-phase heat transfer experiments are given in Table I, where inlet velocity, u_{in}, and effective heat flux, q''_{eff}, were determined from

$$u_{in} = \frac{Q}{NA_c}, \tag{1}$$

$$q''_{eff} = \frac{P_W}{A_t}. \tag{2}$$

During each test, the flow loop components were first adjusted to yield the desired operating conditions. The heat sink was then allowed to reach steady-state, following which the inlet and outlet pressures, P_{in} and P_{out}, outlet temperature, T_{out}, heat sink temperatures, T_{tc1} to T_{tc4}, and heater power, P_W, were measured.

B. Numerical Method

Taking advantage of symmetry, a micro-channel heat sink unit cell containing a single micro-channel and surrounding solid is chosen as shown in Fig. 3. Dimensions of the unit cell are given in Table II.

Heat transfer in the unit cell is a conjugate one combining heat conduction in the solid and convection to the cooling fluid. To simplify the analysis, the following approximations were employed: steady-state laminar flow, constant solid and fluid properties, and negligible natural air convection in the deep slots in the underside of the heat sink. The resulting governing differential equations can be written as follows. For the cooling water

$$\nabla V = 0, \tag{3}$$

$$\rho_f(V \cdot \nabla V) = -\nabla P + \nabla \cdot (\mu_f \nabla V), \tag{4}$$

$$\rho_f c_{P,f}(V \cdot \nabla T) = k_f \nabla^2 T. \tag{5}$$

For the solid regions

$$V = 0, \tag{6}$$

$$k_s \nabla^2 T = 0 \text{ for the copper heat sink,} \tag{7a}$$

$$k_l \nabla^2 T = 0 \text{ for the Lexan cover plate,} \tag{7b}$$

$$k_{air} \nabla^2 T = 0 \text{ for air in the deep slots.} \tag{7c}$$

A uniform velocity and a fully-developed flow are applied at the channel inlet and exit, respectively. Zero velocity is assigned to all other solid boundaries. For thermal boundary conditions, a constant heat flux and constant natural convection coefficient are applied at the unit cell bottom wall (Wall A) and at the unit cell top wall (Wall C), respectively. Adiabatic boundary conditions are applied to all other boundaries of the solid region. For the liquid region, a constant temperature is applied at the

a: Channel Bottom Wall
b: Channel Side Wall
c: Channel Top Wall
A: Unit Cell Bottom Wall
C: Unit Cell Top Wall
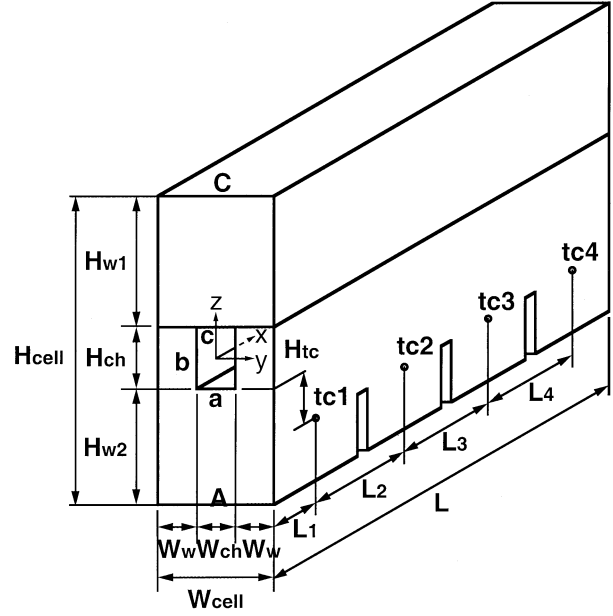
Fig. 3. Micro-channel heat sink unit cell.

TABLE II
DIMENSIONS OF MICRO-CHANNEL HEAT SINK UNIT CELL

W_w (µm)	W_{ch} (µm)	H_{w1} (µm)	H_{ch} (µm)	H_{w2} (µm)	H_{tc} (µm)
118	231	12,700	713	5637	2462

L_1 (mm)	L_2 (mm)	L_3 (mm)	L_4 (mm)		
5	11.588	11.588	11.588		
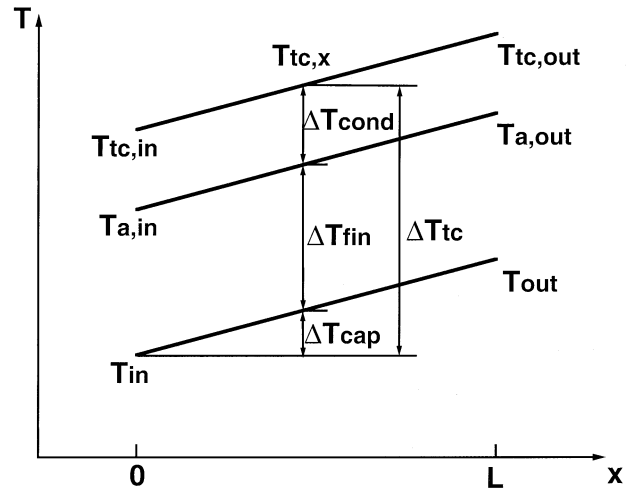
Fig. 4. Schematic of temperature profiles in heat sink unit cell.

channel inlet, and the flow is assumed thermally fully developed at the outlet.

A numerical scheme utilizing the SIMPLE algorithm [24] was developed to solve (3)–(7c) to obtain the temperature field

TABLE III
SUMMARY OF FIN ANALYSIS MODELS

Model No.	Ref.	$Nu\left(=\dfrac{h_{ave}\,d_h}{k_f}\right)$	η	A_{eff}
1	[1]	4.8504	$\dfrac{tanh(m\,H_{ch})}{m\,H_{ch}}$	$2\,\eta\left(A_a + A_b\right)$
2	[2]	$\dfrac{2}{\alpha}\left[1.10 + 0.555\left(Pr_f\,Re\,\dfrac{d_h\,\alpha^2}{4\,L}\right)^{0.55}\right]$		$2\left(A_a + A_b\right)$
3	[8]	$-1.047 + 9.326\dfrac{\alpha^2 + 1}{(\alpha+1)^2}$	$\dfrac{tanh(m\,H_{ch})}{m\,H_{ch}}$	$A_a + 2\,\eta\,A_b$
4	[3]	$\left[\left(2.22\,x*^{-0.33}\right)^3 + Nu_m^{\,3}\right]^{\frac{1}{3}}$ $Nu_m = -0.02 + 8.31\dfrac{\alpha^2+1}{(\alpha+1)^2}$	$\dfrac{tanh(m\,H_{ch})}{m\,H_{ch}}$	$\eta\,A_a + 2\,\eta\,A_b$
5	[9]	$Nu_{x,4}(x*,\alpha)\dfrac{Nu_3(\alpha)}{Nu_4(\alpha)}$ $Nu_{x,4}(x*,\alpha) = 4.8053 + 0.1202\,ln(x*)$ $-0.0505\,ln(x*)^2 - 0.0353\,ln(x*)^3$ $Nu_3(\alpha) = 5.2666,\; Nu_4(\alpha) = 4.8504$	$\dfrac{tanh(m\,H_{ch})}{m\,H_{ch}}$	$A_a + 2\,\eta\,A_b$
6	[10]	$8.235(1 - 1.883\alpha + 3.767\alpha^2$ $-5.814\alpha^3 + 5.361\alpha^4 - 2\alpha^5\,)$		$A_a + 2A_b$
7	[5]	$8.24 - 16.8\alpha + 25.4\alpha^2 - 20.4\alpha^3 + 8.7\alpha^4$ $for\; x* \geq 0.1$ $3.35(x*)^{-0.13}\alpha^{-0.12}\,Pr_f^{-0.038}$ $for\; 0.013 \leq x* \leq 0.1$ $1.87(x*)^{-0.3}\alpha^{-0.056}\,Pr_f^{-0.036}$ $for\; 0.005 \leq x* \leq 0.013$	$\dfrac{tanh(m\,H_{ch})}{m\,H_{ch}}$	$A_a + 2\,\eta\,A_b$
8	[11]	$-1.047 + 9.326\dfrac{\alpha^2 + 1}{(\alpha+1)^2}$	$\dfrac{tanh(m\,H_{ch})}{m\,H_{ch}}$	$2\,\eta\left(A_a + A_b\right)$

within the heat sink unit cell. Details concerning the numerical techniques used when applying the SIMPLE algorithm to a conjugate heat transfer problem are available elsewhere [6], [15], [24], [25].

C. Fin Analysis Method

The fin analysis method is a simplified approach to evaluating the temperature field within the heat sink unit cell. The technique for determining the temperature at the heat sink's thermocouple plane (see Fig. 3) using the fin analysis method is as follows.

After introducing the approximations discussed in Section I, the longitudinal profiles for water bulk temperature, channel bottom wall (Wall a) temperature, and thermocouple plane temperature can be determined as shown in Fig. 4. For a given T_{in},

the thermocouple plane temperature at a longitudinal distance x can be evaluated from

$$T_{tc,x} = T_{in} + \Delta T_{tc} = T_{in} + \left(\Delta T_{cap} + \Delta T_{fin} + \Delta T_{cond}\right)$$
$$= T_{in} + q''_{eff}LW_{cell}\left(R_{cap} + R_{fin} + R_{cond}\right). \qquad (8)$$

R_{cap}, R_{fin}, and R_{cond} are called the capacity resistance, fin resistance, and conduction resistance, respectively, and can be calculated from

$$R_{cap} = \frac{1}{\rho_f c_{p,f} u_{in} A_c}\left(\frac{x}{L}\right), \qquad (9)$$

$$R_{fin} = \frac{1}{h_{ave} A_{eff}}, \qquad (10)$$

$$R_{cond} = \frac{H_{tc}}{k_s LW_{cell}}. \qquad (11)$$

Equations (9)–(11) are adopted in most fin analysis models, though a variety of relations have been proposed for h_{ave} and A_{eff} when evaluating R_{fin}. A summary of these relations is
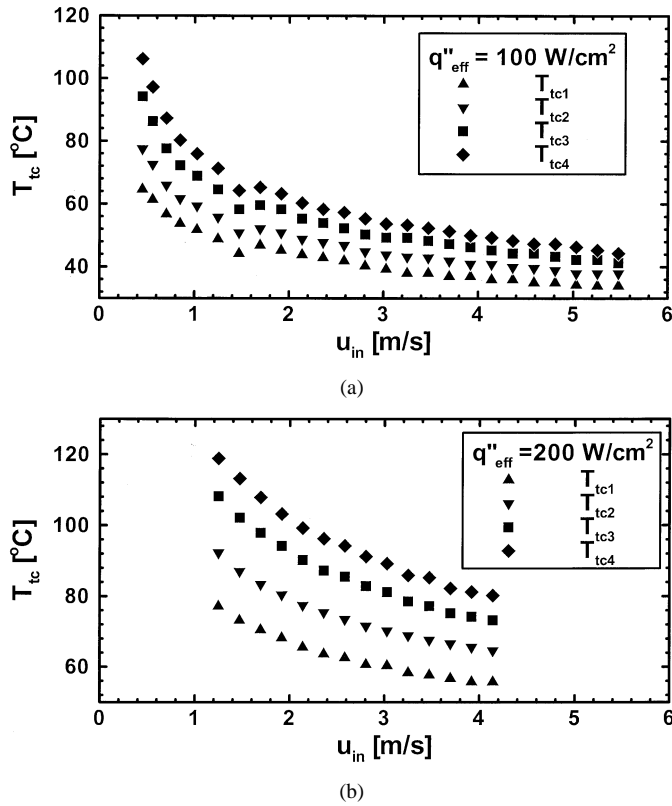
Fig. 5. Thermocouple readings inside micro-channel heat sink versus inlet velocity for (a) $q''_{eff} = 100 \, \mathrm{W/cm^2}$ and (b) $q''_{eff} = 200 \, \mathrm{W/cm^2}$ [15].

Fig. 6. Comparison of experimental data and predictions from numerical simulation and fin analysis models for temperature distribution along thermocouple line at $u_{in} = 2.8 \, \mathrm{m/s}$ for (a) $q''_{eff} = 100 \, \mathrm{W/cm^2}$ and (b) $q''_{eff} = 200 \, \mathrm{W/cm^2}$.

provided in Table III, where x^*, α, and m are the dimensionless thermal entry distance, channel aspect ratio, and fin parameter, respectively

$$x^* = \frac{x}{d_h \mathrm{Re} \, \mathrm{Pr}_f}, \quad \alpha = \frac{W_{ch}}{H_{ch}}, \quad m = \sqrt{\frac{h_{ave}}{k_s W_w}}. \quad (12)$$

D. Results and Discussion

Fig. 5(a) and (b) show the variation of measured temperature (along thermocouple line in Fig. 3) inside the heat sink with inlet velocity u_{in} for two heat fluxes. For each location, the temperature decreases with increasing u_{in}. For the same u_{in}, the temperature increases along the flow direction.

Fig. 6(a) and (b) compare the temperatures measured along the thermocouple line with predictions from both the numerical simulation and fin analysis models listed in Table III for $u_{in} = 2.8 \, \mathrm{m/s}$ and two heat fluxes. The shallow dips in the numerically predicted curves correspond to locations of the deep slots where air is trapped as illustrated in Fig. 3. Fig. 6(a) and (b) prove numerical simulation is the most accurate method. Several fin analysis models, such as models 4, 5, and 7, are also fairly accurate. It can be seen from Table III that models 4, 5, and 7 all employ correlations that account for thermal entrance effects, while the other models utilize thermally fully developed flow correlations. This leads to the important conclusion that only thermally developing flow correlations should be adopted when applying the fin analysis method to model micro-channel heat sinks.

The numerical method predictions for the fluid bulk temperature and the average wall temperatures at the unit cell bottom

wall (Wall A), channel bottom wall (Wall a), channel top wall (Wall c), unit cell top wall (Wall C), and thermocouple plane are plotted in Fig. 7(a) and (b) for $u_{in} = 2.8 \, \mathrm{m/s}$ and two heat fluxes. As expected, the average temperature decreases from the unit cell bottom wall (Wall A) to the unit cell top wall (Wall C). The liquid bulk temperature is lower than all five solid wall planes. The highest unit cell temperatures are encountered near the channel exit; the highest point is located at the unit cell bottom wall (Wall A) immediately below the channel exit. As shown in Section IV, the channel exit is very important to boiling incipience.

IV. BOILING INCIPIENCE IN MICRO-CHANNEL HEAT SINK

A. Experimental Procedure

The operating conditions for the micro-channel boiling incipience experiments are given in Table IV. During each test, the water was first deaerated using an immersion heater situated inside the reservoir. The flow loop components were then adjusted to yield the desired operating conditions. After the flow became stable, the heater power was set to a point well below the incipient boiling heat flux. The power was then increased in small increments while the flow loop components were constantly adjusted to maintain the desired operating conditions. At each power level, the heat sink was allowed to reach steady-state conditions, following which the inlet pressure, P_{in}, outlet temperature, T_{out}, heat sink temperatures, and heater power, P_W, were all measured. The flow inside the micro-channels was vi-
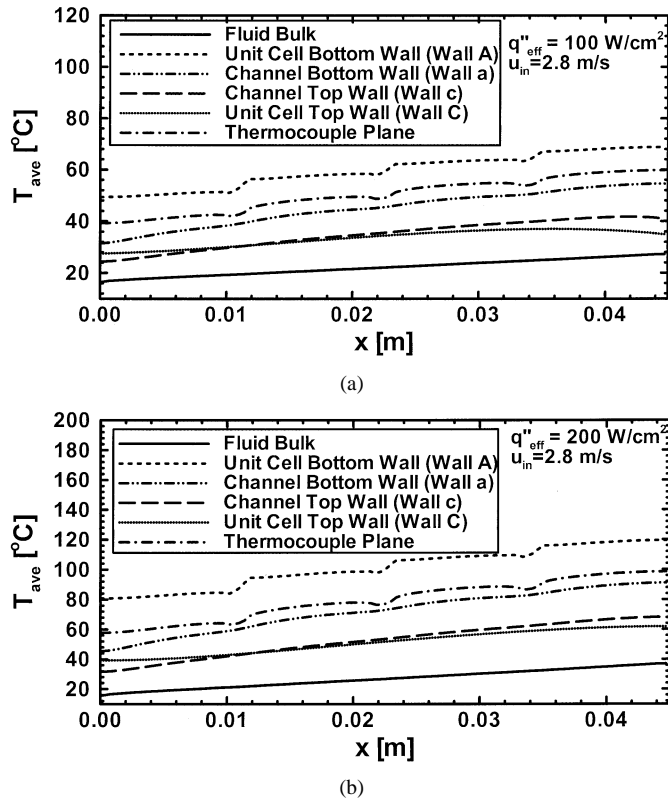
Fig. 7. Numerical predictions of average temperature for $u_{in} = 2.8$ m/s: (a) $q''_{eff} = 100$ W/cm^2 and (b) $q''_{eff} = 200$ W/cm^2 [15].

TABLE IV
OPERATING CONDITIONS FOR BOILING INCIPIENCE TESTS

Cooling liquid	Inlet temperature, T_{in} ($^{\circ}$C)	Inlet velocity, u_{in} (m/s)	Outlet pressure, P_{out} (bar)
Deionized water	30.0	0.13-1.19	1.2
	60.0	0.16-1.34	1.2
	90.0	0.17-1.44	1.2

sually monitored with the aid of the microscope. The effective heat flux measured when the first bubbles appeared inside the micro-channels was defined as the incipient boiling heat flux, $q''_{eff,i}$. At boiling incipience, a small number of nucleation sites appeared simultaneously close to the exit of several (typically five to eight) micro-channels; one or two sites were typically activated per micro-channel. After nucleation, bubbles first grew to detachment size before being entrained into the liquid flow and deposited into the downstream plenum, where they collapsed.

B. Mechanistic Model of Incipient Boiling Heat Flux

A new mechanistic model based on bubble departure criteria is developed to predict the incipient boiling heat flux, $q''_{eff,i}$. The model development is based on the following two assumptions:

1) bubble departure will occur when the liquid drag force exerted on the bubble overcomes the surface tension force;
2) a bubble will only grow and detach if the lowest temperature point along its interface is at least equal to the saturation temperature.
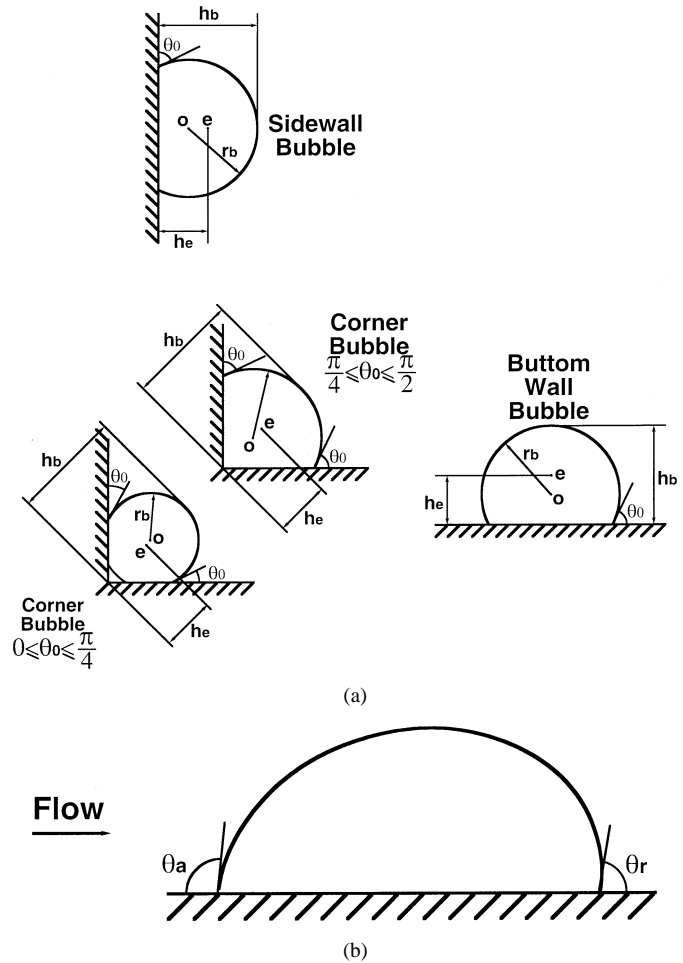
Fig. 8. Appearance of departing bubble (a) at channel cross section and (b) along flow direction.

The observed bubble activities revealed boiling incipience strongly depends on both the hydrodynamic and thermal conditions at the micro-channel exit. A two-dimensional analysis is therefore performed on the exit of the unit cell shown in Fig. 3 to obtain both the velocity and temperature distributions in the liquid.

1) Mechanical Considerations: According to the first assumption of the incipience model, the forces acting on a departing bubble should be in balance. In this model, the assumptions about bubble shape and forces of Al-Hayes and Winterton [26] are adopted and modified to account for the complexities of bubble growth in a rectangular micro-channel. Vapor bubbles are grouped into bottom wall bubbles, sidewall bubbles, and corner bubbles. The bubbles are treated as truncated spheres with contact angles at the wall equal to the equilibrium contact angle θ_0 as illustrated in Fig. 8(a). At the point of bubble departure, the liquid drag force and surface tension forces must balance each other

$$F_d = F_s. \tag{13}$$

The drag force, F_d, is assumed to be proportional to the projected area of the bubble facing the flow and the dynamic pressure of the cooling water, and can be evaluated from [26]

$$F_d = C_d \frac{1}{2} \rho_f u_e^2 A_p \tag{14}$$

where C_d, A_p and u_e are the drag coefficient, projected area of the bubble, and velocity at a point e half-way from the nucleation site to the bubble tip, respectively. For bottom wall and sidewall bubbles

$$A_p = r_b^2(\pi - \theta_0 + \cos\theta_0 \sin\theta_0) \qquad (15)$$

and for corner bubbles

$$A_p = r_b^2(\pi - 2\theta_0 + 2\cos\theta_0 \sin\theta_0) \text{ for}$$
$$0 \leq \theta_0 \leq \frac{\pi}{4}, \qquad (16a)$$
$$\text{and } A_p = r_b^2\left[\frac{3\pi}{4} - \theta_0 + \cos\theta_0 (\cos\theta_0 + \sin\theta_0)\right]$$
$$\text{for } \frac{\pi}{4} \leq \theta_0 \leq \frac{\pi}{2}. \qquad (16b)$$

The drag coefficient C_d is a function of the bubble Reynolds number Re_b [26]

$$C_d = \frac{24}{Re_b} \text{ for } 4 < Re_b < 20, \qquad (17a)$$
$$\text{and } C_d = 1.22 \text{ for } 20 > Re_b < 400 \qquad (17b)$$

where u_e is employed as the characteristic velocity when evaluating C_d

$$Re_b = \frac{\rho_f u_e (2r_b)}{\mu_f}. \qquad (18)$$

The surface tension force is evaluated as

$$F_s = C_s \frac{1}{4}\sigma P_c(\cos\theta_r - \cos\theta_a) \qquad (19)$$

where P_c, θ_r and θ_a are the length of the contact line, receding contact angle and advancing contact angle, respectively. C_s in (19) is an empirical coefficient given by [26]

$$C_s = \frac{58}{\theta_0 + 5} + 0.14 \qquad (20)$$

where θ_0 is in degrees. For bottom wall and sidewall bubbles

$$P_c = 2\pi r_b \sin\theta_0 \qquad (21)$$

and for corner bubbles

$$P_c = 4\pi r_b \sin\theta_0 \text{ for } 0 \leq \theta_0 \leq \frac{\pi}{4}, \qquad (22a)$$
$$\text{and } P_c = 4r_b \sin\theta_0 \left[\pi - \arccos\left(\frac{\cos\theta_0}{\sin\theta_0}\right)\right] \text{ for}$$
$$\frac{\pi}{4} \leq \theta_0 \leq \frac{\pi}{2}. \qquad (22b)$$

θ_a and θ_r are modified contact angles at the bubble upstream and downstream stagnation points, respectively, as illustrated in Fig. 8(b), which can be calculated from the following correlations proposed by Winterton [27] for water

$$\theta_a = \theta_0 + 10°, \qquad (23a)$$
$$\text{and } \theta_r = \theta_0 - 10°. \qquad (23b)$$

Substituting (14) and (19) into (13) and rearranging terms yield, for bottom wall and sidewall bubbles

$$u_e^2 r_b = \frac{C_s}{C_d} \frac{\sigma}{\rho_f} \frac{\pi \sin\theta_0 (\cos\theta_r - \cos\theta_a)}{\pi - \theta_0 + \cos\theta_0 \sin\theta_0} \qquad (24)$$

and for corner bubbles

$$u_e^2 r_b = \frac{C_s}{C_d} \frac{\sigma}{\rho_f} \frac{2\pi \sin\theta_0 (\cos\theta_r - \cos\theta_a)}{\pi - 2\theta_0 + 2\cos\theta_0 \sin\theta_0} \text{ for}$$
$$0 \leq \theta_0 \leq \frac{\pi}{4}, \text{ and} \qquad (25a)$$
$$u_e^2 r_b = \frac{C_s}{C_d} \frac{\sigma}{\rho_f}$$
$$\times \frac{2\left[\pi - \arccos\left(\frac{\cos\theta_0}{\sin\theta_0}\right)\right] \sin\theta_0 (\cos\theta_r - \cos\theta_a)}{\frac{3\pi}{4} - \theta_0 + \cos\theta_0 (\cos\theta_0 + \sin\theta_0)}$$
$$\text{for } \frac{\pi}{4} \leq \theta_0 \leq \frac{\pi}{2}. \qquad (25b)$$

The detailed liquid velocity distribution at the micro-channel exit is required to evaluate u_e. Fully-developed single-phase laminar flow in a rectangular duct is assumed [28] just upstream of the bubble. Given the velocity field, nucleation site position, and all relevant material properties, the radius of a departing bubble, r_b, can be calculated by solving (24), (25a) or (25b). Once r_b is known, the geometry of the bubble can be easily specified.

2) Thermal Considerations: According to the second assumption of the incipience model, the entire bubble interface must be superheated before a bubble can depart. To meet this requirement, the lowest temperature along the bubble's interface should be greater than, or at least equal to the saturation temperature. The temperature distribution around the bubble interface should therefore be determined to identify the lowest temperature point along the interface. This can be accomplished once both the geometry of the departing bubble and the liquid temperature distribution at the channel exit are determined.

The temperature distribution in the liquid can be determined by solving a two-dimensional conjugate heat transfer problem at the exit of the heat sink unit cell. The following dimensionless parameters are introduced:

$$Y = \frac{y}{W_{cell}}, \quad Z = \frac{z}{W_{cell}}$$
$$\theta = \frac{k_s(T - T_{out})}{q''_{eff} W_{cell}}, \quad U = \frac{u}{u_{out}}. \qquad (26)$$

Assuming fully-developed single-phase laminar flow, the energy equation, (5), corresponding to the different regions of the exit unit cell can be nondimensionalized as

$$\frac{k_f}{k_s}\left(\frac{\partial^2\theta}{\partial Y^2} + \frac{\partial^2\theta}{\partial Z^2}\right) = \frac{W_{cell}^2}{A_c} U$$
$$\text{for the liquid region.} \qquad (27)$$
$$\frac{\partial^2\theta}{\partial Y^2} + \frac{\partial^2\theta}{\partial Z^2} = 0 \text{ for the copper heat sink} \qquad (28)$$
$$\text{and } \frac{k_l}{k_s}\left(\frac{\partial^2\theta}{\partial Y^2} + \frac{\partial^2\theta}{\partial Z^2}\right) = 0 \text{ for the Lexan cover plate.} \qquad (29)$$

The boundary condition for Wall A of the unit cell is

$$-\frac{\partial\theta}{\partial Z} = 1 \qquad (30)$$

and all other unit cell boundaries are assumed adiabatic.

A numerical scheme utilizing the finite difference method was developed to solve (27)–(29) to calculate the dimensionless
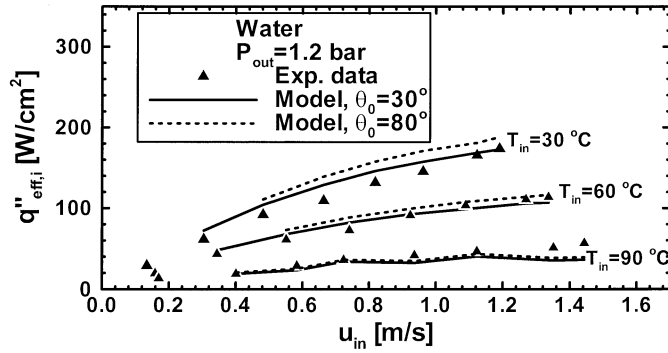
Fig. 9.   Comparison of experimental results and model predictions for incipient boiling heat flux [16].

Fig. 10.   Schematic of flow regions in a micro-channel.

temperature field. Detailes concerning the numerical techniques employed in this model are available elsewhere [16], [24], [25].

3) Procedure to Predict the Incipient Boiling Heat Flux: First, the force balance calculations are performed. u_{out} is set to be equal to the inlet velocity u_{in} due to the small liquid density variations along the micro-channel. The velocity field at the micro-channel exit is then computed using a formula provided in [28]. The bubble departure radius, r_b, is calculated for a large number of nucleate sites equidistantly spaced along the micro-channel wall by solving (24), (25a), or (25b).

Next, the thermal analysis is performed. The dimensionless temperature field, θ, at the heat sink unit cell exit is determined by solving (27)–(29) numerically. A small value is then assigned to q''_{eff}, and the mean exit temperature, T_{out}, is determined from a simple energy balance

$$\rho_f c_{P,f} u_{in} N A_c(T_{out} - T_{in}) = q''_{eff} A_t. \tag{31}$$

The liquid temperature, T, field, is determined by substituting q''_{eff} and T_{out} into the dimensionless temperature, θ, field. Given the bubble departure radius and temperature field at channel exit, the lowest temperature along the bubble interface is calculated for each nucleation site along the micro-channel wall.

The value of heat flux, q''_{eff}, is then increased and thermal analysis repeated until the lowest temperature along the interface of a bubble just exceeds the saturation temperature. The q''_{eff} value for this condition is the incipient boiling heat flux, $q''_{eff,i}$, for the micro-channel heat sink.

C. Model Predictions

Fig. 9 shows the measured incipient boiling heat flux, $q''_{eff,i}$, increases with increasing inlet velocity, u_{in}, and decreasing inlet temperature, T_{in}. Also shown in Fig. 9 are the predictions based on the present model. Two different equilibrium contact angles are assumed, 30 and 80°, due to the variability of contact angle of water on metallic surfaces. Good agreement is shown between the predictions for both angles and the incipient boiling heat flux data, proving the effectiveness of this new model for thermal design of two-phase micro-channel heat sinks. The model is not valid below a minimum u_{in}, which is a function of θ_0, for which bubbles approach the size of the micro-channel cross section. Details concerning this limit can be found in [16].
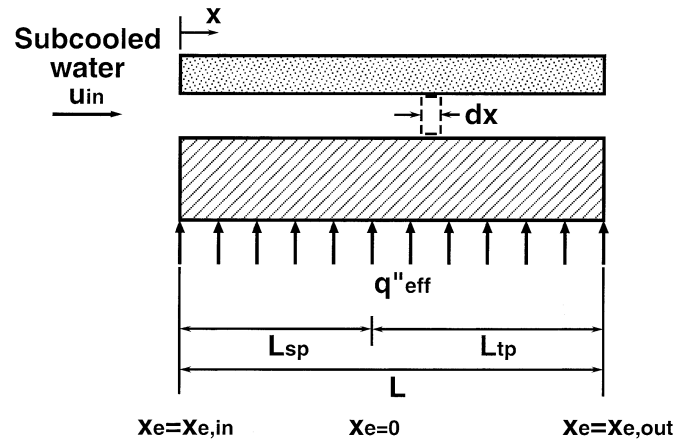
V. PRESSURE DROP IN TWO-PHASE MICRO-CHANNEL HEAT SINK

A. Pressure Drop Model

As shown in Fig. 10, water is supplied into the heat sink subcooled $(T_{in} < T_{sat})$. Heat is transferred from the solid heat sink to the water, which results in a stream-wise increase in the water temperature. Eventually, boiling is initiated inside the micro-channels. The flow from this point to the heat sink exit consists of a two-phase vapor-liquid mixture. For convenience in predicting the pressure drop, the total length of the heat sink, L, is divided into two sections based upon the range of thermodynamic equilibrium quality, x_e. From the subcooled inlet $(x_e < 0)$ to the location of $x_e = 0$ is the single-phase length, L_{sp}. The downstream section begins with zero quality and continues to the heat sink exit $(x_e = x_{e,out})$, and is referred to as the two-phase length, L_{tp}. The total pressure drop across the micro-channel heat sink includes the pressure drops from the single-phase and two-phase regions

$$\Delta P = \Delta P_{sp} + \Delta P_{tp}. \tag{32}$$

The two-phase region is characterized by saturated boiling, which is described using the homogeneous equilibrium model. This model is based on the assumption that liquid and vapor phases form a homogeneous mixture with equal and uniform velocities, and properties are uniform within each phase. Applying conservation of mass, energy, and momentum to the differential control volume shown in Fig. 10 and rearranging terms yield the following equations [19], [29], respectively, where all liquid and vapor properties are functions of local pressure only, as seen in (33) and (34) shown at the bottom of the next page. The numerator in (34) is the sum of the frictional and accelerational components, the latter is the result of heating alone. The denominator of (34) can be expressed as $1 - M^2$, where M is the two-phase Mach number

$$M^2 = -G^2 \frac{v_{fg}}{h_{fg}}(v_f + x_e v_{fg}) - G^2 \left(\frac{dv_f}{dP} + x_e \frac{dv_{fg}}{dP} \right)$$
$$+ \frac{G^2 v_{fg}}{h_{fg}} \left(\frac{dh_f}{dP} + x_e \frac{dh_{fg}}{dP} \right). \tag{35}$$

This Mach number expression is the sum of the following terms, from left to right, respectively, for kinetic energy changes, compressibility, and flashing.

Pressure drop across the two-phase region, ΔP_{tp}, can be calculated by solving the coupled (33) and (34) simultaneously. The fourth-order Runge-Kutta technique is employed to solve these equations.

Two distinct approaches are generally employed to determine the two-phase friction factor f_{tp}. In the first approach, f_{tp} is evaluated using standard single-phase friction factor correlations with the viscosity term replaced by a two-phase mixture viscosity [29]. Different relationships have been proposed for the two-phase viscosity as a function of individual phase viscosities and vapor quality. The degree of success of these relationships depends upon both channel geometry and test conditions. Alternatively, f_{tp} can be estimated directly from measured two-phase pressure drop; a value in the range of 0.0029 to 0.0033 was suggested for low pressure flashing steam-water flow [29]. A recent study by Bowers and Mudawar [19] indicated a value of $f_{tp} = 0.003$ provides excellent agreement between predictions of the homogeneous equilibrium model and their pressure drop data for R-113 flow boiling in a heat sink with circular micro-channels. The value of 0.003 is therefore assumed for f_{tp} in the present study as well.

For the single-phase region of the channel, a fully developed flow is assumed. This may underestimate the single-phase pressure drop by neglecting the developing flow pressure drop as well as the inlet and exit pressure losses. However, the pressure drop within the single-phase region is much smaller than the two-phase region (as will be discussed later), and the error introduced is small. Therefore, the pressure drop across the single-phase region can be evaluated from

$$\Delta P_{sp} = \frac{2 f_{sp} G^2 L_{sp}}{\rho_f d_h} \qquad (36)$$

where an appropriate single-phase friction factor f_{sp} for laminar flow in a rectangular channel with smooth walls is employed [28].

B. Results and Discussion

A test case is analyzed here to help illustrate the various parametric influences for two-phase micro-channel heat sinks. Water is used as the cooling fluid and an inlet velocity of 0.34 m/s, inlet pressure of 1.5 bar, and effective heat flux of 200 W/cm^2 are assumed.

Fig. 11(a) shows the predicted pressure distribution along the two-phase micro-channel. The pressure changes are small in the
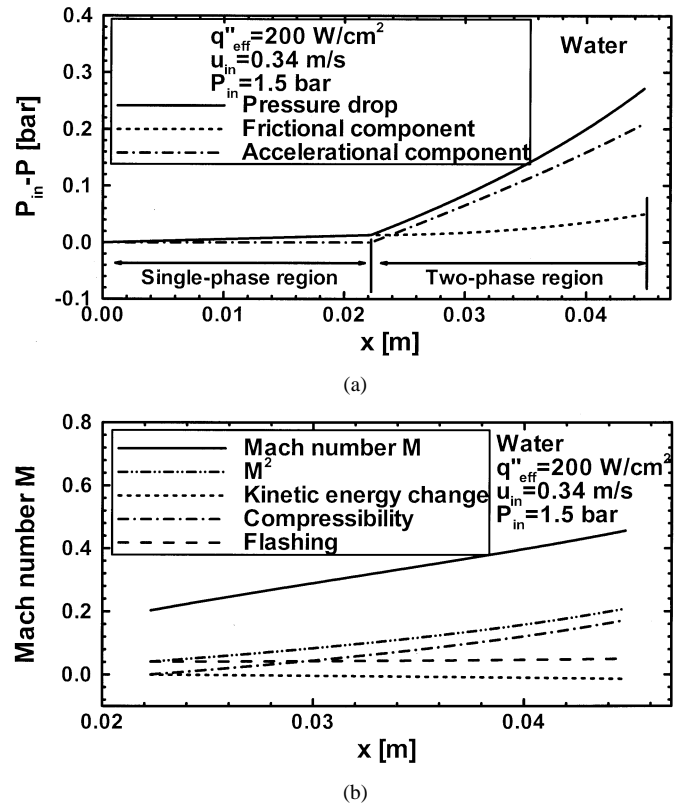
Fig. 11. (a) Pressure drop distribution along micro-channel. (b) Two-phase Mach number distribution along micro-channel.

single-phase region and increase considerably in the two-phase region. Further analysis indicates that the larger pressure drop within the two-phase region is due mostly to the accelerational effect represented by the second term in the numerator of (35). This accelerational effect is the result of a significant increase in flow velocity in the two-phase region caused by the reduction in average density that accompanies the vapor production.

The property variations with pressure also contribute to pressure loss within the two-phase region, which accounts for the nonlinear behavior of the pressure gradient. The axial distribution of two-phase Mach number is presented in Fig. 11(b). The Mach number increases monotonically along the flow direction. Fig. 11(b) also shows the individual contributions of kinetic energy changes, compressibility, and flashing to the Mach number. For the conditions studied, compressibility plays the most dominant role.

Fig. 12 shows the variation of pressure drop across the heat sink with inlet velocity. Pressure starts increasing with increasing velocity for small inlet velocities, then decreases, and

$$\frac{dx_e}{dx} = \frac{\frac{q''_{eff} W_{cell}}{G A_c} + \left[G^2 \left(v_f + x_e v_{fg} \right) \left(\frac{dv_f}{dP} + x_e \frac{dv_{fg}}{dP} \right) + \left(\frac{dh_f}{dP} + x_e \frac{dh_{fg}}{dP} \right) \right] \left(-\frac{dP}{dx} \right)}{h_{fg} + G^2 v_{fg} \left(v_f + x_e v_{fg} \right)} \qquad (33)$$

$$-\left(\frac{dP}{dx} \right) = \frac{\left[1 + \frac{G^2 v_{fg}}{h_{fg}} \left(v_f + x_e v_{fg} \right) \right] \left(\frac{2 f_{tp} G^2 v_f}{d_h} \right) \left[1 + x_e \frac{v_{fg}}{v_f} \right] + \left(\frac{q''_{eff} W_{cell}}{G A_c} \right) \frac{G^2 v_{fg}}{h_{fg}}}{1 + G^2 \frac{v_{fg}}{h_{fg}} \left(v_f + x_e v_{fg} \right) + G^2 \left(\frac{dv_f}{dP} + x_e \frac{dv_{fg}}{dP} \right) - \frac{G^2 v_{fg}}{h_{fg}} \left(\frac{dh_f}{dP} + x_e \frac{dh_{fg}}{dP} \right)}. \qquad (34)$$
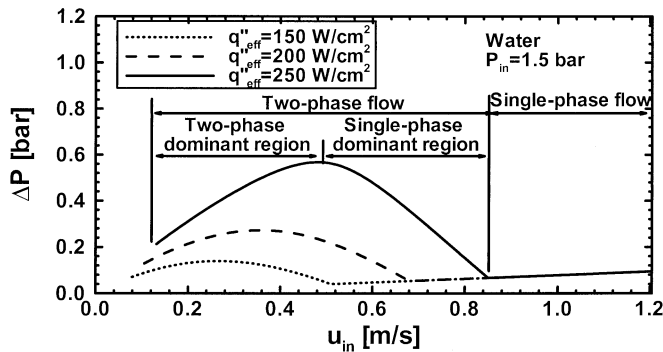
Fig. 12. Effects of water inlet velocity and effective heat flux on pressure drop.

eventually increases again. As discussed earlier, pressure drop in the two-phase region is much higher than in the single-phase region. With a very small inlet velocity, two-phase flow will prevail over a greater portion of the micro-channel length. The significant vapor production causes large accelerational pressure losses that are responsible for the initial increase in pressure drop. However, with increasing inlet velocity, the single-phase length begins increasing, and the pressure drop lowering effect of the single-phase region becomes even more dominant. When inlet velocity becomes large, the flow inside the micro-channels is comprised of single-phase liquid, where pressure drop increases rather mildly with increasing inlet velocity. Fig. 12 also shows the pressure drop increases significantly in the two-phase region with increasing effective heat flux.

The above results prove this model is a simple tool for thermal design of two-phase micro-channel heat sinks. More importantly, it is quite effective at predicting the unique features of two-phase pressure drop such as flashing, compressibility, and choking, which few other more complicated models are capable of tackling. The model has been successful at predicting flow boiling pressure drop of R-113 in a heat sink containing 510 μm circular micro-channels [17], [19]. On the other hand, a recent study by Mukherjee and Mudawar [30] revealed several fundamental differences in flow boiling behavior in micro-channels between water and FC-72; the latter is a fluorochemical coolant with thermophysical properties fairly similar to those of R-113. Their results reveal the low surface tension and small contact angle of fluorochemicals produce bubble departure diameters that are one to two orders of magnitude smaller than those for water. These new findings point to a need to further explore the validity of the homogeneous equilibrium model with a systematic database for water flow boiling in micro-channels. Such experiments are the focus of several ongoing studies at PUIECA. A more comprehensive assessment of the predictive capabilities of different pressure drop models, including the homogeneous equilibrium model, is available in a separate paper by the authors [31].

VI. CONCLUSION

In this study, several fundamental and practical aspects of single-phase and two-phase micro-channel heat sinks are addressed. Key findings are as follows.

1) The heat transfer characteristics of a single-phase micro-channel heat sink were investigated both experimentally and theoretically. A comparison between experimental results and predictions based on both numerical simulation and fin analysis models was presented. It is shown that, while numerical simulation offers the most accurate predictions, a few of the simple fin analysis models also provide fairly accurate results. All the successful fin models employ heat transfer correlations that account for thermal entrance effects, while the less successful ones utilize thermally fully developed flow correlations.

2) The incipient boiling heat flux increases with increasing inlet velocity and decreasing inlet temperature. A mechanistic model was constructed to predict the incipient boiling heat flux. The model is based on a bubble departure criterion, which accounts for both force balance on a bubble and superheat requirement for entire bubble interface. This model is capable of predicting the size of bubbles departing from both the flat surfaces and corner regions of a rectangular micro-channel, the temperature field around the bubble interface, and the location of the first bubble to depart. The model predictions are in good agreement with the incipient boiling heat flux data.

3) An analytical model is developed to predict pressure drop across a two-phase micro-channel heat sink. The homogeneous equilibrium model is applied to the two-phase region, while fully developed flow is assumed in the single-phase region. The pressure changes are small in the single-phase region and increase considerably in the two-phase region. The large pressure drop within the two-phase region is due mostly to two-phase acceleration. Property variations with pressure result in a nonlinear variation of pressure gradient in the two-phase region, and may result in two-phase choking.

REFERENCES

[1] D. B. Tuckerman and R. F. W. Pease, "High-performance heat sinking for VLSI," *IEEE Electron. Devices Lett.*, vol. EDL-2, pp. 126–129, May 1981.

[2] T. Kishimito and T. Ohsaki, "VLSI packaging technique using liquid-cooled channels," *IEEE Trans. Comp., Hybrids, Manufact. Technol.*, vol. CHMT-9, pp. 328–335, Dec. 1986.

[3] D. Copeland, H. Takahira, W. Nakayama, and B. C. Pak, "Manifold microchannel heat sinks: Theory and experiment," in *Advances Electronic Packaging*. New York: ASME, 1995, vol. EEP-10, pp. 829–835.

[4] K. Kawano, K. Minakami, H. Iwasaki, and M. Ishizuka, "Micro channel heat exchanger for cooling electrical equipment," in *Proc. ASME Heat Transfer Div.*, vol. HTD-361-3/PID-3, 1998, pp. 173–180.

[5] T. M. Harms, M. J. Kazmierczak, and F. M. Cerner, "Developing convective heat transfer in deep rectangular microchannels," *Int. J. Heat Fluid Flow*, vol. 20, no. 2, pp. 149–157, Apr. 1999.

[6] W. Qu and I. Mudawar, "Experimental and numerical study of pressure drop and heat transfer in a single-phase micro-channel heat sink," *Int. J. Heat Mass Transfer*, vol. 45, no. 12, pp. 2549–2565, June 2002.

[7] R. J. Phillips, "Micro-channel heat sinks," in *Advances in Thermal Modeling of Electronic Components*. New York: ASME Press, 1990, vol. 2, pp. 109–184.

[8] R. W. Knight, D. J. Hall, J. S. Goodling, and R. C. Jaeger, "Heat sink optimization with application to microchannels," *IEEE Trans. Comp., Hybrids, Manufact. Technol.*, vol. 15, pp. 832–842, Oct. 1992.

[9] S. F. Choquette, M. Faghri, M. Charmchi, and Y. Asako, "Optimum design of microchannel heat sinks," in *Micro-Electro-Mechanical Systems (MEMS)*. New York: ASME, 1996, vol. DSC-59, pp. 115–126.

[10] H. H. Bau, "Optimization of conduits' shape in micro heat exchangers," *Int. J. Heat Mass Transfer*, vol. 41, no. 18, pp. 2717–2723, Sep. 1998.

[11] D. Y. Lee and K. Vafai, "Comparative analysis of jet impingement and microchannel cooling for high heat flux applications," *Int. J. Heat Mass Transfer*, vol. 42, no. 9, pp. 1555–1568, May 1999.

[12] A. Weisberg, H. H. Bau, and J. N. Zemel, "Analysis of microchannels for integrated cooling," *Int. J. Heat Mass Transfer*, vol. 35, no. 10, pp. 2465–2474, Oct. 1992.

[13] X. Yin and H. H. Bau, "Uniform channel micro heat exchangers," *J. Electron. Packag.*, vol. 119, no. 2, pp. 89–93, June 1997.

[14] A. G. Fedorov and R. Viskanta, "Three-dimensional conjugate heat transfer in the microchannel heat sink for electronic packaging," *Int. J. Heat Mass Transfer*, vol. 43, no. 3, pp. 399–415, Feb. 2000.

[15] W. Qu and I. Mudawar, "Analysis of three-dimensional heat transfer in micro-channel heat sinks," *Int. J. Heat Mass Transfer*, vol. 45, no. 19, pp. 3973–3985, Sept. 2002.

[16] ——, "Prediction and measurement of incipient boiling heat flux in micro-channel heat sinks," *Int. J. Heat Mass Transfer*, vol. 45, no. 19, pp. 3933–3945, Sept. 2002.

[17] M. B. Bowers and I. Mudawar, "High flux boiling in low flow rate, low pressure drop mini-channel and micro-channel heat sinks," *Int. J. Heat Mass Transfer*, vol. 37, no. 2, pp. 321–332, Jan. 1994.

[18] ——, "Two-phase electronic cooling using mini-channel and micro-channel heat sinks: Part 1—Design criteria and heat diffusion constraints," *J. Electron. Packag.*, vol. 116, no. 4, pp. 290–297, Dec. 1994.

[19] ——, "Two-phase electronic cooling using mini-channel and micro-channel heat sinks: Part 2—Flow rate and pressure drop constraints," *J. Electron. Packag.*, vol. 116, no. 4, pp. 298–305, Dec. 1994.

[20] L. Zhang, J. M. Koo, L. Jiang, S. S. Banerjee, M. Ashegi, K. E. Goodson, J. G. Santiago, and T. W. Kenny, "Measurement and modeling of two-phase flow in microchannels with nearly-constant heat flux boundary conditions," *Micro-Electro-Mech. Syst. (MEMS)*, vol. MEMS-2, pp. 129–135, 2000.

[21] L. Jiang, M. Wong, and Y. Zohar, "Forced convection boiling in a microchannel heat sink," *J. Microelectromech. Syst.*, vol. 10, no. 1, pp. 80–87, Mar. 2001.

[22] X. F. Peng and B. X. Wang, "Forced convection and flow boiling heat transfer for liquid flowing through microchannels," *Int. J. Heat Mass Transfer*, vol. 36, no. 14, pp. 3421–3427, Sept. 1993.

[23] T. S. Ravigururajan, "Impact of channel geometry on two-phase flow heat transfer characteristics of refrigerants in microchannel heat exchangers," *J. Heat Transfer*, vol. 120, no. 2, pp. 485–491, May 1998.

[24] S. V. Patankar, *Numerical Heat Transfer and Fluid Flow*. Washington, DC: Hemisphere, 1980.

[25] ——, "A numerical method for conduction in composite materials, flow in irregular geometries and conjugate heat transfer," in *Proc. 6th Inte. Heat Transfer Conf.*, vol. 3, 1978, pp. 297–302.

[26] R. A. M. Al-Hayes and R. H. S. Winterton, "Bubble diameter in detachment in flowing liquids," *Int. J. Heat Mass Transfer*, vol. 24, no. 2, pp. 223–230, Feb. 1981.

[27] R. H. S. Winterton, "Flow boiling: Prediction of bubble departure," *Int. J. Heat Mass Transfer*, vol. 27, no. 8, pp. 1422–1424, Aug. 1984.

[28] R. K. Shah and A. L. London, *Laminar Flow Forced Convection in Ducts: A Source Book for Compact Heat Exchanger Analytical Data*. New York: Academic, 1978.

[29] J. G. Collier and J. R. Thome, *Convective Boiling and Condensation*, 3rd ed. Oxford, U.K.: Oxford Univ. Press, 1994.

[30] S. Mukherjee and I. Mudawar, "Pumpless loop for narrow channel and micro-channel boiling," *J. Electron. Packag.*, to be published.

[31] W. Qu and I. Mudawar, "Measurement and prediction of pressure drop in two-phase micro-channel heat sinks," *Int. J. Heat Mass Transfer*, vol. 46, pp. 2739–2753, 2003.

Weilin Qu received the B.E. and M.S. degrees from Tsinghua University, China, in 1994 and 1997, respectively, and is currently pursuing the Ph.D. degree at Boiling and Two-Phase Flow Laboratory, School of Mechanical Engineering, Purdue University, West Lafayette, IN.

His research concerns experimental study, theoretical modeling, and numerical analysis of the various transport phenomena associated with single-phase liquid flow and forced convective boiling in micro-channels.

Issam Mudawar received the M.S. and Ph.D. degrees from the Massachusetts Institute of Technology, Cambridge, in 1980 and 1984, respectively.

His graduate work involved magnetohydrodynamic (MHD) energy conversion and phase-change water cooling of turbine blades. He joined the School of Mechanical Engineering, Purdue University, West Lafayette, IN, in 1984, where he established and became Director of the Boiling and Two-Phase Flow Laboratory (BTPFL) and Electronic Cooling Research Center (ECRC). He also served as Chairman of the Heat Transfer Area at Purdue University. His work has been focused on phase change processes, thermal management of electronic and aerospace devices, intelligent materials processing, and nuclear reactor safety. His theoretical and experimental research encompasses sensible and evaporative heating of thin films, pool boiling, flow boiling, jet-impingement cooling, spray cooling, micro-channel heat sinks, heat transfer enhancement, heat transfer in rotating systems, critical heat flux, capillary pumped flows, and surface rewetting. His Electronic Cooling Research Center was renamed in 1998 as the Purdue University International Electronic Cooling Alliance (PUIECA), where efforts are presently focussed entirely on high-heat-flux cooling schemes. He is also President of Mudawar Thermal Systems, Inc. (a firm that is dedicated to the development of thermal solutions to computer and aerospace systems).

Dr. Mudawar received the Best Paper Award in Electronic Cooling at the 1988 National Heat Transfer Conference, the Best Paper Award in Thermal Management at the 1992 ASME/JSME Joint Conference on Electronic Packaging, the *Journal of Electronic Packaging* Outstanding Paper of the Year Award for 1995, the Solberg Award for Best Teacher in School of Mechanical Engineering (1987, 1992 and 1996), the Charles Murphy Award for Best Teacher at Purdue University (1997), and the National Society of Black Engineers Professor of the Year Award (1985, 1987). He is a Fellow of the American Society of Mechanical Engineers.